Real-Time Cycle Slip Detection and Repair Method for BDS-3 Five-Frequency Data

HAIJUN YUAN[ID]**1, ZHETAO ZHANG**[ID]**1, XIUFENG HE**[ID]**1, TIANYANG XU**[1]**, XUEYONG XU**[2]**, AND NAN ZANG**[3]

[1]School of Earth Sciences and Engineering, Hohai University, Nanjing 211100, China
[2]Northern Information Control Research Academy Group Company Ltd., Nanjing 211153, China
[3]College of Intelligent Systems Science and Engineering, Harbin Engineering University, Harbin 150001, China

Corresponding author: Xiufeng He (xfhe@hhu.edu.cn)

ABSTRACT Theoretically, five-frequency observations can form combined observations with longer wavelength, smaller ionospheric delay and smaller noise, which may improve the performance of cycle slip detection and repair. Four geometry-free phase combinations and one geometry-free phase and pseudorange combination are formed to detect and repair the cycle slips in real time. Firstly, the high-quality geometry-free phase combinations of three, four and five frequencies are discussed, then the optimal five-frequency geometry-free phase combinations are selected to detect the cycle slips. Secondly, one geometry-free phase and pseudorange combination which is linearly independent with the above four phase combinations is added to ensure that all the cycle slips can be detected. Thirdly, a real-time cycle slip repair algorithm based on the LAMBDA search method is deduced. The five-frequency real-time cycle slip detection and repair method has been tested by using BDS-3 undifferenced data, even under the condition of active ionospheric and low sampling interval. The results showed that the proposed method is capable of detecting and repairing all the simulated cycle slips on the five carriers in real time.

INDEX TERMS Cycle slip detection and repair, BDS-3, five-frequency, geometry-free phase combination, geometry-free phase and pseudorange combination.

I. INTRODUCTION

The phenomenon of cycle slip inevitably occurs because of the temporary failure of lock in the GNSS receiver carrier tracking loop, low signal-to-noise ratio, active ionosphere or high receiver dynamics. Whatever the reason for the cycle slips, such undesirable discontinuities should be detected and repaired before the carrier phase observations are used in GNSS high-precision positioning applications, such as precise point positioning and real-time kinematic positioning [1], [2].

Cycle slip detection and repair is an indispensable part of GNSS data processing. Accordingly, there are many methods to detect and repair the cycle slips in the past few decades. The Turbo Edit method is widely used to detect the cycle slips and

The associate editor coordinating the review of this manuscript and approving it for publication was Seung-Hyun Kong[ID].

it essentially combines the geometry-free (GF) combination and HMW combination [3]. The Turbo Edit method has been applied in many famous softwares, such as PANDA and Bernese [4], [5]. But it cannot repair the cycle slips and could be insensitive in case of active ionospheric or large pseudorange noise. Therefore, some studies have improved the Turbo Edit method. Liu [6] replaced the GF combination with the ionospheric total electron content rate (TECR) to detect the cycle slips, but the method should be used under the condition of 1 Hz or even higher sampling rate. Cai *et al.* [7] presented a forward and backward moving window averaging (FBMWA) method integrated with the second-order time-differenced phase ionospheric residual (STPIR) method based on the Turbo Edit method. However, it cannot be used to detect the cycle slips in real time. In addition, De Lacy *et al.* [8] proposed a cycle slip detection method based on the Bayesian theory, while it is constrained by high

sampling rate. The integration method of GNSS and INS data is also used for cycle slip detection [9], while the cost of the INS system greatly constrains its feasibility in many applications. Banville and Langley [10] presented a cycle slip detection algorithm based on the geometry-based (GB) model and tested its performance under the condition of different ionospheric. Li *et al.* [11] proposed a undifferenced cycle slip repair method based on the GB model for real-time precise point positioning (PPP). Li *et al.* [12] further presented a geometry-based ionospheric-weighted (GBIW) approach to repair the cycle slips for multi-GNSS and multi-frequency observations under the condition of active ionospheric and data gaps.

Along with the availability of multi-frequency signals of GNSS systems, a new upsurge is aroused for triple-frequency cycle slip detection and repair method. In theory, triple-frequency signals can be capable of improving the ability to detect the cycle slips [13]. Zhang and Li [14] also verified the performance of triple-frequency cycle slip detection can be significantly improved than dual-frequency. Dai *et al.* [15] presented an integration method of two geometry-free phase combinations and the classical LAMBDA method to detect and repair the cycle slips, while it cannot detect some insensitive cycle slips. Huang *et al.* [16] applied two geometry-free phase combinations and one geometry-free phase and pseudorange combination to detect and repair the cycle slips. However, the mentioned methods are not necessarily effective under the condition of active ionospheric and large sampling interval. Chang *et al.* [17] applied adaptive kalman filter based on variance component estimation to predict the ionospheric delays and aid the cycle slip repair for GNSS triple-frequency signals. Zhao *et al.* [18] and Li *et al.* [19] took the ionospheric delays between epochs into consideration in narrow-lane cycle slip identification. However, five frequencies are currently available, covering the B1C (1575.420 MHz), B1I (1561.098 MHz), B3I (1268.520 MHz), B2b (1207.140 MHz) and B2a (1176.450 MHz) signals of BeiDou navigation satellite system (BDS-3) and E1 (1575.420 MHz), E5a (1176.450 MHz), E5b (1207.140 MHz), E5 (1191.795 MHz) and E6 (1278.750 MHz) of the Galileo. It has been verified that the increasement of frequencies can exert greater advantages. Zhang *et al.* [20] verified that the four frequencies can improve the success rate of ambiguity resolution. Both Li *et al* [21] and Jin and Su [22] find that the four frequencies can benefit the high-precision positioning, such as RTK and PPP. But the multi-frequency cycle slip detection is an important prerequisite for their work. In addition, the five-frequency combination observations can form combined observations with longer wavelength, smaller ionospheric delay and smaller noise, which may improve the performance of cycle slip detection. It is valuable to discuss the performance of cycle slip detection with five frequencies, while few scholars have studied the method and advantage of the BDS-3 five-frequency cycle slip detection and repair.

In this contribution, we will propose a real-time cycle slip detection and repair method for BDS-3 five-frequency data. The rest of the paper is organized as follows, in Section II, the geometry-free phase combination theory is presented. Meanwhile, we discuss the high-quality geometry-free phase combinations of three, four and five frequencies, select four joint geometry-free phase combinations which have lower noise and lower ionospheric effect in Section III. Then, one geometry-free phase and pseudorange combination is added and the detection sensitivity with different pseudorange noise is discussed in Section IV. In addition, a real-time cycle slip repair method based on the LAMBDA search algorithm is presented in Section V. Further, the performance of the real-time cycle slip detection and repair method is investigated under different situations in Section VI. Finally, the conclusions are drawn in Section VII.

II. CYCLE SLIP DETECTION USING FIVE-FREQUENCY GEOMETRY-FREE PHASE COMBINATIONS

The carrier phase and code observation at epoch t_0 can be expressed as

$$P_i(t_0) = \rho(t_0) + t_r(t_0) - t^s(t_0) + \xi^s_{r,i}(t_0) + T(t_0)$$
$$+ \theta_i I'_1(t_0) + \varepsilon_{P_i}(t_0) \tag{1}$$

$$\lambda_i \varphi_i(t_0) = \rho(t_0) + t_r(t_0) - t^s(t_0) + \varsigma^s_{r,i}(t_0) + T(t_0)$$
$$+ \lambda_i N_i(t_0) - \lambda_i \vartheta_i I_1(t_0) + \varepsilon_{\varphi_i}(t_0) \tag{2}$$

with

$$\theta_i = \frac{f_1^2}{f_i^2} \tag{3}$$

$$\vartheta_i = \frac{f_1}{f_i} \tag{4}$$

where the superscript s denotes the satellite, and the subscripts r and i ($i = 1, 2, 3, 4, 5$) denote the receiver and frequency, respectively; P, λ and φ denote code observation, carrier phase wavelength and carrier phase observation, respectively; ρ denotes the range between the receiver and satellite; t_r and t^s denote the receiver and satellite clock errors, respectively; $\xi^s_{r,i}$ and $\varsigma^s_{r,i}$ denote the code and phase hardware delays, respectively; I'_1 and I_1 denote the ionospheric delays scaled to meters and cycles on the B1C signal. $\theta_i, \vartheta_i, \varepsilon_{P_i}$ and ε_{φ_i} denote the respective ionospheric delays amplification factors, code and phase observation noises, respectively; T, N and f denote the troposphere delays, integer ambiguity and signal frequency, respectively.

Based on the multi-frequency combination observations theory, assuming that the coefficients $\alpha, \beta, \gamma, \delta$ and ζ satisfy the condition $\alpha + \beta + \gamma + \delta + \zeta = 0$, the five-frequency geometry-free phase combination observation at epoch t_0 can

be expressed as

$$
\begin{aligned}
&\alpha\lambda_1\varphi_1(t_0) + \beta\lambda_2\varphi_2(t_0) + \gamma\lambda_3\varphi_3(t_0) + \delta\lambda_4\varphi_4(t_0) \\
&\quad + \zeta\lambda_5\varphi_5(t_0) \\
&= -\eta I_1(t_0) + \alpha\lambda_1 N_1(t_0) + \beta\lambda_2 N_2(t_0) + \gamma\lambda_3 N_3(t_0) \\
&\quad + \delta\lambda_4 N_4(t_0) + \zeta\lambda_5 N_5(t_0) + \varsigma(t_0) + \varepsilon(t_0)
\end{aligned} \tag{5}
$$

with

$$
\eta = \alpha\lambda_1 + \frac{\beta\lambda_2 f_1}{f_2} + \frac{\gamma\lambda_3 f_1}{f_3} + \frac{\delta\lambda_4 f_1}{f_4} + \frac{\zeta\lambda_5 f_1}{f_5} \tag{6}
$$

$$
\begin{aligned}
\varsigma(t_0) &= \alpha\varsigma_{r,1}^s(t_0) + \beta\varsigma_{r,2}^s(t_0) + \gamma\varsigma_{r,3}^s(t_0) \\
&\quad + \delta\varsigma_{r,4}^s(t_0) + \zeta\varsigma_{r,5}^s(t_0)
\end{aligned} \tag{7}
$$

$$
\begin{aligned}
\varepsilon(t_0) &= \alpha\lambda_1\varepsilon_1(t_0) + \beta\lambda_2\varepsilon_2(t_0) + \gamma\lambda_3\varepsilon_3(t_0) \\
&\quad + \delta\lambda_4\varepsilon_4(t_0) + \zeta\lambda_5\varepsilon_5(t_0)
\end{aligned} \tag{8}
$$

where η represents the ionospheric delays amplification factor of the geometry-free phase combination; ς and ε denote the hardware delays and the noises of the combination observation.

Hence, the combination observation is only affected by the ionospheric delays, equipment delays and noises. Assuming that a cycle slip group $(\Delta N_1, \Delta N_2, \Delta N_3, \Delta N_4, \Delta N_5)$, where ΔN_i denotes the cycle slip value on the φ_i signal, occurs. Differencing Eq. (5) between adjacent epochs, the combination observation equation can be deduced as follows

$$
\begin{aligned}
&\alpha\lambda_1\Delta\varphi_1 + \beta\lambda_2\Delta\varphi_2 + \gamma\lambda_3\Delta\varphi_3 + \delta\lambda_4\Delta\varphi_4 + \zeta\lambda_5\Delta\varphi_5 \\
&= -\eta\Delta I_1 + \alpha\lambda_1\Delta N_1 + \beta\lambda_2\Delta N_2 + \gamma\lambda_3\Delta N_3 + \delta\lambda_4\Delta N_4 \\
&\quad + \zeta\lambda_5\Delta N_5 + \Delta\varsigma + \Delta\varepsilon
\end{aligned} \tag{9}
$$

Because the equipment delays usually vary slowly with time, the equipment delay $\Delta\varsigma$ is small enough to be ignored compared with the combination observation noise. Therefore, Eq. (9) is only affected by the ionospheric delays $-\eta\Delta I_1$ and noises $\Delta\varepsilon$. Since the ionospheric delays and noises depend on the coefficients $\alpha, \beta, \gamma, \delta$ and ζ. One optimal detection combination should reduce the ionospheric delays and noises as much as possible. Hence, the coefficients should be selected such that $\alpha\lambda_1 + \beta\lambda_2 f_1/f_2 + \gamma\lambda_3 f_1/f_3 + \delta\lambda_4 f_1/f_4 + \zeta\lambda_5 f_1/f_5 \rightarrow 0$ and $(\alpha\lambda_1)^2 + (\beta\lambda_2)^2 + (\gamma\lambda_3)^2 + (\delta\lambda_4)^2 + (\zeta\lambda_5)^2 \rightarrow 0$. Under the condition of quite ionosphere or high sampling rate, the value of ΔI_1 is small. When the η is also small enough, the $\eta\Delta I_1$ can be ignored.

Assuming that the carrier phase observations have the identical standard deviation σ_φ, the standard deviation of Eq. (9) is expressed as

$$
\begin{aligned}
&\sigma_{\alpha\beta\gamma\delta\zeta} \\
&= \sqrt{2}\sqrt{(\alpha\lambda_1)^2 + (\beta\lambda_2)^2 + (\gamma\lambda_3)^2 + (\delta\lambda_4)^2 + (\zeta\lambda_5)^2}\,\sigma_\varphi
\end{aligned} \tag{10}
$$

Because $\sigma_{\alpha\beta\gamma\delta\zeta}$ is generally supposed to be a normal distribution, we can take Eq. (11) to judge whether a cycle slip occurs

$$
\begin{aligned}
&|\alpha\lambda_1\Delta\varphi_1 + \beta\lambda_2\Delta\varphi_2 + \gamma\lambda_3\Delta\varphi_3 + \delta\lambda_4\Delta\varphi_4 + \zeta\lambda_5\Delta\varphi_5| \\
&\qquad\qquad\qquad\qquad \geq \mu\sigma_{\alpha\beta\gamma\delta\zeta}
\end{aligned} \tag{11}
$$

To further improve the reliability, we can take $\mu = 4$ (99.9 % confidence level) as the threshold coefficient to judge whether a cycle slip occurs. When the condition Eq. (11) is satisfied at the current epoch, it can be concluded that a certain cycle slip has occurred.

III. SELECTION OF OPTIMAL FIVE-FREQUENCY GEOMETRY-FREE PHASE COMBINATIONS

According to the preceding discussion, a typical geometry-free phase combination observation may highly be affected by ionospheric delays and noises. Therefore, an ideal geometry-free phase detection combination should satisfy the following conditions in order to have a higher sensitivity for cycle slip detection.

$$
\begin{aligned}
&\alpha + \beta + \gamma + \delta + \zeta = 0 \\
&\min\left(\alpha\lambda_1 + \frac{\beta\lambda_2 f_1}{f_2} + \frac{\gamma\lambda_3 f_1}{f_3} + \frac{\delta\lambda_4 f_1}{f_4} + \frac{\zeta\lambda_5 f_1}{f_5}\right) \\
&\min\left((\alpha\lambda_1)^2 + (\beta\lambda_2)^2 + (\gamma\lambda_3)^2 + (\delta\lambda_4)^2 + (\zeta\lambda_5)^2\right)
\end{aligned} \tag{12}
$$

It should be emphasized that the larger the coefficients $\alpha, \beta, \gamma, \delta$ and ζ are, the larger the value $\mu\sigma_{\alpha\beta\gamma\delta\zeta}$ and the combination noises. When the value $\sigma_{\alpha\beta\gamma\delta\zeta}$ is too large for some combinations, certainly the small cycle slips cannot be detected. Hence, the values of the coefficients $\alpha, \beta, \gamma, \delta$ and ζ are searched within the range of -5 to 5 in order to reduce the combination noises.

Obviously, there are infinite selections for geometry-free phase combination depending on the different values of combination coefficients. Hence, the optimal combinations can be selected according to certain conditions such that the lower ionospheric delays and lower combination noises can be obtained. In order to analyze the theoretical optimal combination, we can further compare the properties of different combination observations. BDS-3 three frequencies usually refer to B1C, B3I and B2a signals; four frequencies usually refer to B1C, B1I, B3I and B2a signals [23], [24]. The cycle slip detection is mainly affected by ionospheric delays, we further define the high-quality combinations which satisfy the conditions of ionospheric delays amplification factor $|\eta| < 0.1$ and the combination observation noises $\sigma < 0.05$. At this time, the ionospheric delays and combination observation noises are reduced to a great extent. Some similar definitions can also be found in [25], [26]. According to the statistics, the total number of high-quality combinations with three, four and five frequencies which satisfy the above conditions are 14, 154 and 1438, respectively. It can be clearly found that the more frequencies, the more numbers of high-quality combinations. Therefore, there are more high-quality combinations to select for the cycle slip detection with the increasement of frequencies.

Table 1 lists the optimal high-quality geometry-free phase combination of three, four and five frequencies, which has the smallest ionospheric delays amplification factor or noises. It is clearly that the optimal high-quality geometry-free phase combination has a small ionospheric delays amplification

TABLE 1. The best high-quality geometry-free phase combinations of BDS-3 three, four and five frequencies.

	B1C	B1I	B3I	B2b	B2a	η	σ
Three-frequency	1	/	-3	/	2	-0.0077	0.0126
	0	/	1	/	-1	-0.0477	0.0049
Four-frequency	1	-2	3	/	-2	0.0007	0.0138
	1	-1	0	/	0	-0.0035	0.0038
Five-frequency	4	-5	1	5	-5	**0.00002**	0.0307
	1	-1	0	0	0	-0.0035	**0.0038**

TABLE 2. BDS-3 five-frequency geometry-free phase combinations.

$[\alpha, \beta, \gamma, \delta, \zeta]$	η	$\sigma_{\alpha\beta\gamma\delta\zeta}$	$< 4\sigma_{\alpha\beta\gamma\delta\zeta}$
[4, -5, 1, 5, -5]	-0.00002	0.0307	191
[1, -1, 1, -3, 2]	0.0001	0.0137	206
[-4, 4, 1, -2, 1]	0.0006	0.0175	330
[-3, 2, 4, -2, -1]	0.0013	0.0183	186
[2, -1, -4, 2, 1]	0.0022	0.0167	178
[3, -2, -3, -1, 3]	0.0024	0.0180	199
[3, -3, -1, 2, -1]	0.0030	0.0143	194
[1, -2, 1, 1, -1]	0.0791	0.0086	201

factor and noises, which is beneficial to improve the cycle slip detection performance. In addition, the five-frequency high-quality combination has the smallest ionospheric delays amplification factor and noises. Therefore, the cycle slip detection performance should be better with the increasement of frequencies. The five-frequency geometry-free phase combinations should be better than the commonly used dual, three and four-frequency combinations in terms of cycle slip detection capability and the impact of ionospheric delay reduction.

However, the cycle slip detection methods based on combination observation all have the insensitive cycle slip groups. When the size of cycle slips on the five signals are approximately proportional to the combination coefficients, the combination observation differencing value is close to 0, which is difficult to detect. Assuming that a cycle slip group $(\Delta N_1, \Delta N_2, \Delta N_3, \Delta N_4, \Delta N_5)$ occurs in a certain epoch, the differencing value of geometry-free combination observation is $|\alpha\lambda_1\Delta N_1+\beta\lambda_2\Delta N_2+\gamma\lambda_3\Delta N_3+\delta\lambda_4\Delta N_4+\zeta\lambda_5\Delta N_5|$. We can take Eq. (13) to judge the insensitive cycle slip group.

$$|\alpha\lambda_1\Delta N_1 + \beta\lambda_2\Delta N_2 + \gamma\lambda_3\Delta N_3 + \delta\lambda_4\Delta N_4 + \zeta\lambda_5\Delta N_5|$$
$$< 4\sigma_{\alpha\beta\gamma\delta\zeta} \quad (13)$$

Some five-frequency combination observations may have smaller noise, but they can detect the cycle slips only occur on two, three or four signals. Since they cannot detect the cycle slips that only occur on the other signals, the number of the insensitive cycle slip groups is larger than that of other combinations. For example, the number of the insensitive cycle slip groups of combination $[1, -1, 0, 0, 0]$ is 1295 within the range of $(0, 0, 0, 0, 1)$ to $(5, 5, 5, 5, 5)$, but the combination $[4, -5, 1, 5, -5]$ is only 191. In this case, the inequality $\alpha\beta\gamma\delta\zeta \neq 0$ should be enforced to get a five-frequency cycle slip detection combination in order to reduce the insensitive cycle slip groups. With the $\sigma_\varphi = 0.01$ cycles and $\mu = 4$ assumed, the BDS-3 geometry-free phase combinations are given in Table 2. The number of the insensitive cycle slip groups of every combination is counted within the range of $(0, 0, 0, 0, 1)$ to $(5, 5, 5, 5, 5)$ and shown as the fourth column in Table 2.

Table 2 shows that the noises of all the combinations are less than 0.04 cycles, which is much smaller than 1 cycle. Therefore, the small cycle slips can be detected by every combination given in the Table 2. It is clearly that every combination inevitably has some insensitive cycle slip groups, but different combination has different insensitive cycle slip groups. Hence, four combinations are applied to detect the cycle slips in order to reduce the insensitive cycle slip groups. Any four combinations in Table 2 are selected to yield the joint combinations, which have no cycle slip groups within the range of $(0, 0, 0, 0, 1)$ to $(50, 50, 50, 50, 50)$ and lower ionospheric delays as shown in Table 3.

All the cycle slips within the range of $(0, 0, 0, 0, 1)$ to $(50, 50, 50, 50, 50)$ cycles can be detected by all the joint combinations in Table 3. We finally select joint combinations $[4, -5, 1, 5, -5] [1, -2, 1, 1, -1] [1, -1, 1, -3, 2] [-4, 4, 1, -2, 1]$ to

TABLE 3. Joint combinations for the cycle slip detection and the number of insensitive cycle slip groups.

Joint combinations	< 50
[4, -5, 1, 5, -5] [1, -2, 1, 1, -1] [1, -1, 1, -3, 2] [-4, 4, 1, -2, 1]	0
[4, -5, 1, 5, -5] [1, -2, 1, 1, -1] [1, -1, 1, -3, 2] [-3, 2, 4, -2, -1]	0
[4, -5, 1, 5, -5] [1, -2, 1, 1, -1] [-4, 4, 1, -2, 1] [-3, 2, 4, -2, -1]	0
[4, -5, 1, 5, -5] [1, -2, 1, 1, -1] [1, -1, 1, -3, 2] [2, -1, -4, 2, 1]	0
[4, -5, 1, 5, -5] [1, -2, 1, 1, -1] [1, -1, 1, -3, 2] [3, -2, -3, -1, 3]	0
[4, -5, 1, 5, -5] [1, -2, 1, 1, -1] [-4, 4, 1, -2, 1] [2, -1, -4, 2, 1]	0
[4, -5, 1, 5, -5] [1, -2, 1, 1, -1] [1, -1, 1, -3, 2] [3, -3, -1, 2, -1]	0
[4, -5, 1, 5, -5] [1, -2, 1, 1, -1] [-4, 4, 1, -2, 1] [3, -3, -1, 2, -1]	0
[4, -5, 1, 5, -5] [1, -2, 1, 1, -1] [-3, 2, 4, -2, -1] [2, -1, -4, 2, 1]	0
[4, -5, 1, 5, -5] [1, -2, 1, 1, -1] [-3, 2, 4, -2, -1] [3, -2, -3, -1, 3]	0
[4, -5, 1, 5, -5] [1, -2, 1, 1, -1] [-3, 2, 4, -2, -1] [3, -3, -1, 2, -1]	0
[4, -5, 1, 5, -5] [1, -2, 1, 1, -1] [2, -1, -4, 2, 1] [3, -2, -3, -1, 3]	0
[4, -5, 1, 5, -5] [1, -2, 1, 1, -1] [2, -1, -4, 2, 1] [3, -3, -1, 2, -1]	0

detect the cycle slips for five-frequency data, which have the smallest ionospheric delays among all the joint combinations. In addition, the ionospheric delays amplification factor η of the combination $[4, -5, 1, -5, 5]$ is -0.00002, which is almost equal to ionospheric-free (IF) combination. Therefore, the combination can be capable of detecting the cycle slips in ionospheric active cases. Since the five-frequency geometry-free phase combination is capable of forming up to four linear independent combinations, a five-frequency geometry-free phase and pseudorange combination should be added to detect the cycle slips and form five linear independent combinations.

IV. CYCLE SLIP DETECTION USING FIVE-FREQUENCY GEOMETRY-FREE PHASE AND PSEUDORANGE COMBINATION

According to the theory of multi-frequency combination observations, the five-frequency geometry-free phase and pseudorange combination observations can be expressed as follows

$$P_{abcde} = aP_1 + bP_2 + cP_3 + dP_4 + eP_5$$
$$= \rho + \eta_{abcde}I_1' + T + t_{\mathrm{r}} - t^{\mathrm{s}} + \xi_{abcde} + \varepsilon_{abcde} \quad (14)$$

$$\lambda_{ijkmn}\varphi_{ijkmn} = \lambda_{ijkmn}(i\varphi_1 + j\varphi_2 + k\varphi_3 + m\varphi_4 + n\varphi_5)$$
$$= \rho + \lambda_{ijkmn}N_{ijkmn} - \eta_{ijkmn}\lambda_{ijkmn}I_1 + T + t_{\mathrm{r}} - t^{\mathrm{s}}$$
$$+ \varsigma_{ijkmn} + \varepsilon_{ijkmn} \quad (15)$$

with

$$\xi_{abcde} = a\xi_{r,1}^s + b\xi_{r,2}^s + c\xi_{r,3}^s + d\xi_{r,4}^s + e\xi_{r,5}^s \quad (16)$$
$$\varepsilon_{abcde} = a\varepsilon_{P_1} + b\varepsilon_{P_2} + c\varepsilon_{P_3} + d\varepsilon_{P_4} + e\varepsilon_{P_5} \quad (17)$$
$$\varsigma_{ijkmn} = i\varsigma_{r,1}^s + j\varsigma_{r,2}^s + k\varsigma_{r,3}^s + m\varsigma_{r,4}^s + n\varsigma_{r,5}^s \quad (18)$$
$$\varepsilon_{ijkmn} = i\varepsilon_{\varphi_1} + j\varepsilon_{\varphi_2} + k\varepsilon_{\varphi_3} + m\varepsilon_{\varphi_4} + n\varepsilon_{\varphi_5} \quad (19)$$

where a, b, c, d and e denote code combination coefficients $(a, b, c, d, e \in R, a + b + c + d + e = 1)$,

i, j, k, m and n denote carrier phase combination coefficients $(i, j, k, m, n \in Z)$. Then, differencing the carrier phase and pseudorange combination observation, which can be expressed as follows

$$N_{ijkmn} = \varphi_{ijkmn} - \frac{P_{abcde}}{\lambda_{ijkmn}} - \kappa I_1 + \varepsilon' \quad (20)$$

where N_{ijkmn} refers to the combination observation integer ambiguity, κ and ε' denote the ionospheric delays amplification factor and combination observation noises, respectively. Then, differencing Eq. (20) between adjacent epochs, which is deduced as follows

$$\Delta N_{ijkmn} = N_{ijkmn}(t_1) - N_{ijkmn}(t_0)$$
$$= \Delta\varphi_{ijkmn} - \frac{\Delta P_{abcde}}{\lambda_{ijkmn}} - \kappa\Delta I_1 + \Delta\varepsilon' \quad (21)$$

Since the equipment delay usually varies slowly within a short time, the equipment delay is small enough to be ignored compared with the combination observation noises. The cycle slip detection is mainly affected by $\kappa\Delta I_1$ and the value of ΔI_1 is small under the condition of quite ionosphere or high sampling rate. The $\eta\Delta I_1$ can further be ignored with a smaller ionospheric delay amplification factor η. Assuming that σ_φ and σ_P are the carrier phase and pseudorange noises, respectively. The noise $\sigma_{\Delta N_{ijkmn}}$ of Eq. (21) can be expressed as (22), shown at the bottom of the next page.

Similarly, we can define $4\sigma_{\Delta N_{ijkmn}}$ to justify the occurrence of the cycle slips. The smaller the noise $\sigma_{\Delta N_{ijkmn}}$, the higher the detection sensitivity can be obtained. To minimize $\sigma_{\Delta N_{ijkmn}}$, the value of $a^2 + b^2 + c^2 + d^2 + e^2$ should be decreased, while the value of λ_{ijkmn} should be increased. Therefore, we set $a = b = c = d = e = 1/5$ to minimize the pseudorange noise with the relation $a^2 + b^2 + c^2 + d^2 + e^2 \geq \frac{(a+b+c+d+e)^2}{5} \geq 5(abcde)^{\frac{2}{5}}$. In addition, the geometry-free phase and pseudorange combination must be linear independent with the above four geometry-free phase combinations. Accordingly, all the cycle slips can be detected by using the five combinations. In order to further

TABLE 4. BDS-3 five-frequency geometry-free phase and pseudorange combinations.

$[i, j, k, m, n]$	λ_{ijkmn}	κ	$\sigma_{\Delta N_{ijkmn}}$		
			$\sigma_P = 0.3$ m	$\sigma_P = 1.0$ m	$\sigma_P = 3.0$ m
[-2, 2, 2, -5, 3]	146.5261	-0.0209	0.0959	0.0960	0.0968
[1, -1, -1, 3, -2]	20.9323	-0.0068	0.0573	0.0641	0.1068
[1, -1, 1, -3, 2]	20.9323	0.0452	0.0573	0.0641	0.1068
[-1, 1, 1, -2, 1]	18.3158	-0.0277	0.0413	0.0528	0.1110
[1, -1, -1, 4, -3]	6.6603	-0.0412	0.0801	0.1209	0.2945
[1, -1, 0, 1, -1]	6.6603	-0.0152	0.0401	0.0991	0.2863
[1, -1, 1, -2, 1]	6.6603	0.0108	0.0491	0.1030	0.2877
[-1, 1, 2, -4, 2]	6.3707	-0.0361	0.0780	0.1227	0.3064

compare the detection sensitivity with the different pseudorange noise, the conditions of $\sigma_\varphi = 0.01$ cycles and $\sigma_P = 0.3$ m, 1.0 m and 3.0 m are discussed. Some optimal geometry-free phase and pseudorange combinations are selected and listed in Table 4.

Table 4 suggests that all the five-frequency geometry-free phase and pseudorange combinations have an extra-wide lane and their noises are smaller than 0.1 cycles when $\sigma_P = 0.3$ m. But the detection sensitivity of every combination is different with the different pseudorange noise. The combination $[-2, 2, 2, -5, 3]$ has the longest wavelength and the best ability to resist pseudorange noise, which is reflected in the smallest variation of $\sigma_{\Delta N_{ijkmn}}$ under the different noises. In addition, the κ of all the combinations is smaller than 0.05, which can considerably reduce the influence of the ionospheric delays. For example, when the ionospheric delay variation between epochs is less than 0.65 m, and then its effect to the combination [1, -1, 0, 1, -1] is smaller than 0.01 cycles ($0.65 \times 0.0152 < 0.01$).

V. METHODOLOGY OF REAL-TIME CYCLE SLIP REPAIR

When a cycle slip is detected at a certain epoch, the cycle slip value should be calculated. The floating value of the cycle slip can be computed as follows

$$AX = L \qquad (23)$$

with

$$A = \begin{bmatrix} \alpha_1\lambda_1 & \beta_1\lambda_2 & \gamma_1\lambda_3 & \delta_1\lambda_4 & \zeta_1\lambda_5 \\ \alpha_2\lambda_1 & \beta_2\lambda_2 & \gamma_2\lambda_3 & \delta_2\lambda_4 & \zeta_2\lambda_5 \\ \alpha_3\lambda_1 & \beta_3\lambda_2 & \gamma_3\lambda_3 & \delta_3\lambda_4 & \zeta_3\lambda_5 \\ \alpha_4\lambda_1 & \beta_4\lambda_2 & \gamma_4\lambda_3 & \delta_4\lambda_4 & \zeta_4\lambda_5 \\ i & j & k & m & n \end{bmatrix} \qquad (24)$$

$$X = \begin{bmatrix} \Delta N_1 & \Delta N_2 & \Delta N_3 & \Delta N_4 & \Delta N_5 \end{bmatrix}^T \qquad (25)$$

where, l_{φ_i} and l_{P_i} refer to the raw phase and pseudorange observations, respectively. $(\alpha_i, \beta_i, \gamma_i, \delta_i, \zeta_i)$ denote the

coefficients of the geometry-free carrier phase combinations, (i, j, k, m, n) and $(\frac{-a}{\lambda_{ijkmn}}, \frac{-b}{\lambda_{ijkmn}}, \frac{-c}{\lambda_{ijkmn}}, \frac{-d}{\lambda_{ijkmn}}, \frac{-e}{\lambda_{ijkmn}})$ are the phase combination and pseudorange combination coefficients of the geometry-free phase and pseudorange combination, respectively. The covariance matrix Q of L can be expressed as

$$Q = BQ_0B^T \qquad (27)$$

with

$$Q_0 = diag\left(q_{\varphi_1}, q_{\varphi_2}, q_{\varphi_3}, q_{\varphi_4}, q_{\varphi_5}, q_{P_1}, q_{P_2}, q_{P_3}, q_{P_4}, q_{P_5}\right) \qquad (28)$$

where q_{φ_i} and q_{P_i} denote the variance of phase and pseudorange observation, respectively. Assuming that $\sigma_\varphi = 0.01$ cycles and $\sigma_P = 0.3$ m, the least squares estimate for $\hat{X}$ can be expressed as

$$\hat{X} = \left(A^T PA\right)^{-1} A^T PL, P = Q^{-1} \qquad (29)$$

Since the matrix A is non-singular, this estimation can also be written as

$$\hat{X} = A^{-1}L \qquad (30)$$

After the cycle slip floating value is calculated by Eq. (30), we can get the cycle slip value by rounding directly, but the cycle slip value may not be correct because of the influence of the observation noise and the condition number of the coefficient matrix A, which could be ill-conditioned in the processing of matrix inversion. Considering these disadvantages, we have to take the following steps.

Firstly, we should select the proper geometry-free phase and pseudorange combination from the table 4 in order to make the condition number of the matrix A as small as possible. Therefore, we finally select the detection combination $[1, -1, 0, 1, -1]$, which has the smallest condition number value 407.58. Meanwhile, it has the smaller ionospheric delays amplification factor and combination noise.

$$\sigma_{\Delta N_{ijkmn}} = \sqrt{2}\sqrt{\left(i^2 + j^2 + k^2 + m^2 + n^2\right)\sigma_\varphi^2 + \frac{\left(a^2 + b^2 + c^2 + d^2 + e^2\right)\sigma_P^2}{\lambda_{ijkmn}^2}} \qquad (22)$$

TABLE 5. The size and the location of the insensitive cycle slip groups of every combination.

No.	Detection combination	The location of cycle slip/epoch	The insensitive cycle slip groups
1	[4, -5, 1, 5, -5]	2000	(0, 0, 0, 1, 1)
2	[1, -2, 1, 1, -1]	4000	(0, 0, 1, 1, 2)
3	[1, -1, 1, -3, 2]	6000	(0, 1, 3, 2, 2)
4	[-4, 4, 1, -2, 1]	8000	(1, 1, 1, 2, 3)
5	[1, -1, 0, 1, -1]	10000	(2, 2, 2, 2, 2)

Secondly, we can further use a more reliable algorithm, and such search method like LAMBDA is used to get the correct cycle slip groups on the original five carrier phase observations [27]. The optimization of LAMBDA search satisfies the following condition

$$\min\left((z - \hat{z})^{\mathrm{T}} Q_{\hat{z}}^{-1} (z - \hat{z})\right) \tag{31}$$

with

$$z = Z^T X, \quad \hat{z} = Z^T \hat{X}, \; Q_{\hat{z}} = Z^T Q_{\hat{X}} Z \tag{32}$$

where Z is the so-called Z-transformation matrix and $Q_{\hat{z}}$ is covariance matrix after transformation.

Thirdly, the equation (31) maybe does not guarantee the correct cycle slip have been found. But the correct cycle slip correction X must satisfy the condition as follows

$$\min(V^T P V) \tag{33}$$

where $V = AX - L$. If the cycle slip correction X is not correct, then V will be much larger and $V^T P V \neq min$. Hence, the correct cycle slip can be obtained from the condition (33). In addition, after the raw carrier phase data are corrected by the correct cycle slip values, the differencing values of all the five detection combinations will not exceed the corresponding detection threshold, which can further guarantee the correct cycle slips have been found.

VI. DATA TEST AND ANALYSIS

A. EXPERIMENT ONE

The four geometry-free phase joint combinations [4, −5, 1, 5, −5] [1, −2, 1, 1, −1] [1, −1, 1, −3, 2] [−4, 4, 1, −2, 1] and one geometry-free phase and pseudorange combination [1, −1, 0, 1, −1] are selected to detect and repair the cycle

slips, which are marked as Nos. 1, 2, 3, 4 and 5, respectively. The experiment selects BDS-3 five-frequency observation data of a station on the roof of a building, November 14, 2020, as an example and the data sampling interval is 1 s. Since the BDS-3 GEO satellites do not have five-frequency signals, we select the satellites C20 (MEO) and C39 (IGSO). Simulated typical insensitive cycle slip groups are added to the raw five-frequency data of the two satellites in order to verify the effectiveness of the cycle slip detection method. The value and location of every combination insensitive cycle slip group is listed in Table 5.

Figure 1 and Figure 2 depict the differencing value of the satellites C20 and C39 cycle slip detection combinations when no cycle slip occurs. The upper and lower red lines indicate the detection threshold of the corresponding combinations. It can be found that the differencing value is a curve that varies within a certain range and has not exceeded the cycle slip detection threshold, which indicates no cycle slip occurs. In addition, the fluctuation range of the geometry-free phase combinations after differencing is ±0.03 cycles, which is smaller than that of the geometry-free phase and pseudorange combination (±0.04 cycles).

Figure 3 and Figure 4 illustrate the differencing value of the satellites C20 and C39 cycle slip detection combinations when insensitive cycle slip occurs, respectively. It can be found that the differencing value will obviously varies and exceeds the cycle slip detection threshold when an insensitive cycle slip group is added to a certain epoch, which indicates the cycle slip occurs in this epoch. In addition, the insensitive cycle slip group (0, 0, 0, 1, 1) cannot be detected by combination 1, 2, 5, but the other combinations can detect the cycle slip. The cycle slip group (0, 0, 1, 1, 2) is insensitive to detect by using combination 2, but the other combinations

$$L = \underbrace{\begin{bmatrix} \alpha_1\lambda_1 & \beta_1\lambda_2 & \gamma_1\lambda_3 & \delta_1\lambda_4 & \zeta_1\lambda_5 & 0 & 0 & 0 & 0 & 0 \\ \alpha_2\lambda_1 & \beta_2\lambda_2 & \gamma_2\lambda_3 & \delta_2\lambda_4 & \zeta_2\lambda_5 & 0 & 0 & 0 & 0 & 0 \\ \alpha_3\lambda_1 & \beta_3\lambda_2 & \gamma_3\lambda_3 & \delta_3\lambda_4 & \zeta_3\lambda_5 & 0 & 0 & 0 & 0 & 0 \\ \alpha_4\lambda_1 & \beta_4\lambda_2 & \gamma_4\lambda_3 & \delta_4\lambda_4 & \zeta_4\lambda_5 & 0 & 0 & 0 & 0 & 0 \\ i & j & k & m & n & \frac{-a}{\lambda_{ijkmn}} & \frac{-b}{\lambda_{ijkmn}} & \frac{-c}{\lambda_{ijkmn}} & \frac{-d}{\lambda_{ijkmn}} & \frac{-e}{\lambda_{ijkmn}} \end{bmatrix}}_{B} \begin{bmatrix} l_{\varphi_1} \\ l_{\varphi_2} \\ l_{\varphi_3} \\ l_{\varphi_4} \\ l_{\varphi_5} \\ l_{P_1} \\ l_{P_2} \\ l_{P_3} \\ l_{P_4} \\ l_{P_5} \end{bmatrix} \tag{26}$$
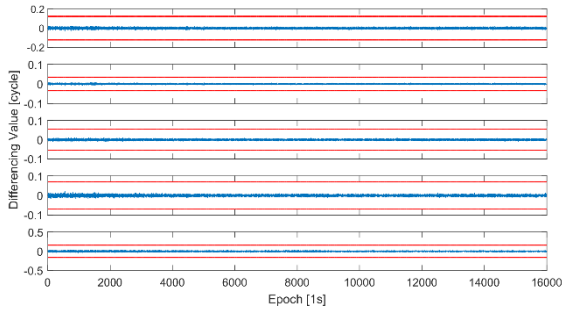
FIGURE 1. Differencing value of the cycle slip detection combinations for the satellite C20 when no cycle slip occurs. The panels from top to bottom denote the combinations Nos. 1, 2, 3, 4 and 5, respectively.
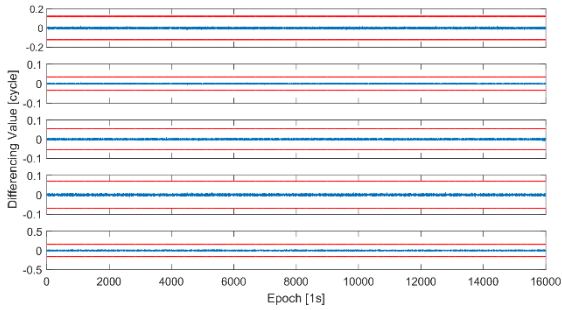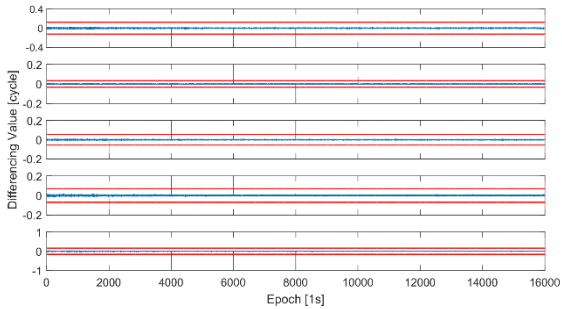

FIGURE 2. Differencing value of the cycle slip detection combinations for the satellite C39 when no cycle slip occurs. The panels from top to bottom denote the combinations Nos. 1, 2, 3, 4 and 5, respectively.

FIGURE 3. Differencing value of the cycle slip detection combinations for the satellite C20 when insensitive cycle slip occurs. The panels from top to bottom denote the combinations Nos. 1, 2, 3, 4 and 5, respectively.

FIGURE 4. Differencing value of the cycle slip detection combinations for the satellite C39 when insensitive cycle slip occurs. The panels from top to bottom denote the combinations Nos. 1, 2, 3, 4 and 5, respectively.

FIGURE 5. Differencing value of the cycle slip detection combinations for the satellite C20. The panels from top to bottom denote the combinations Nos. 1, 2, 3, 4 and 5, respectively.

FIGURE 6. Differencing value of the cycle slip detection combinations for the satellite C39. The panels from top to bottom denote the combinations Nos. 1, 2, 3, 4 and 5, respectively.

can detect the cycle slip. The insensitive cycle slip groups (0, 1, 3, 2, 2) and (1, 1, 1, 2, 3) cannot be detected by combination 3 and 4, respectively, but the other combinations can detect the cycle slip. The equal cycle slip group (2, 2, 2, 2, 2) cannot be detected by combinations 1, 3, 4 and 5, but combination 2 can detect the cycle slip. Hence, it can be concluded that there are some insensitive cycle slip groups undetectable only by one, two, three or four detection combinations, but the insensitive cycle slip groups can be fully detected by using four geometry-free phase combinations and one geometry-free phase and pseudorange combination.

B. EXPERIMENT TWO

The experiment test data is selected as same as experiment one. In order to further verify the applicability of the proposed real-time cycle slip detection and repair method, the cycle
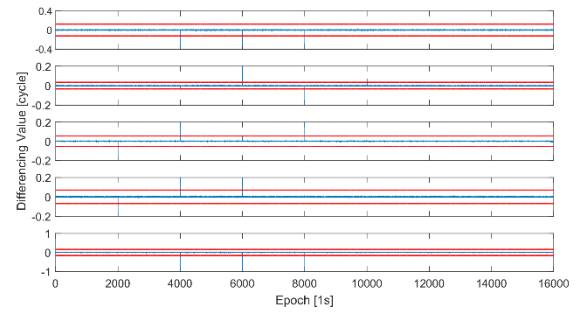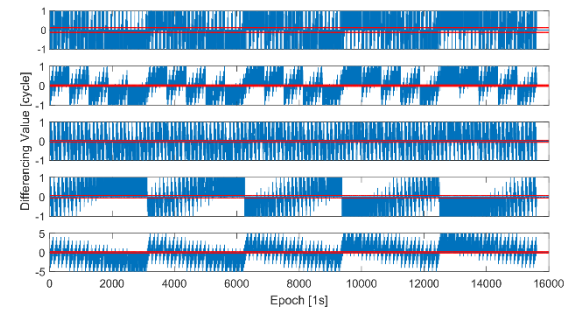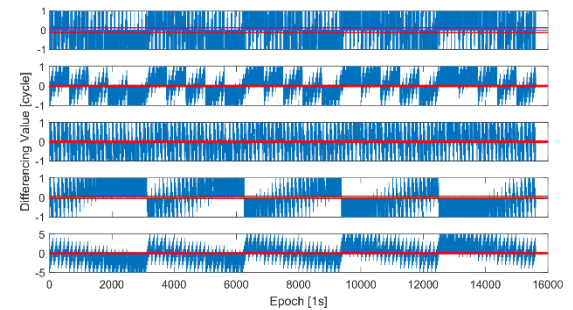
slip groups within the range of (0, 0, 0, 0, 1) to (4, 4, 4, 4, 4) with an interval of 5 epochs are added to the raw carrier phase data of the satellites C20 and C39, a total of 3124 cycle slip groups.

Figure 5 and Figure 6 depict the differencing value of the cycle slip detection combinations for the satellites C20 and C39, respectively. The differencing value of the cycle slip detection combinations will exceed the detection threshold (shown as the red lines) when the cycle slip occurs. According to statistics, the results show that the proposed method can detect all the cycle slips.

Then the LAMBDA search method is used to repair the cycle slips in real time. The cycle slip detection and repair success rate results of the satellites C20 and C39 are shown in Table 6 by rounding directly and using the LAMBDA

TABLE 6. The real-time cycle slip detection and repair success rate of the satellites C20 and C39.

PRN	Cycle slip detection success rate	Cycle slip repair success rate	
		Round	LAMBDA
C20	100 %	94.65 %	100 %
C39	100 %	97.18 %	100 %

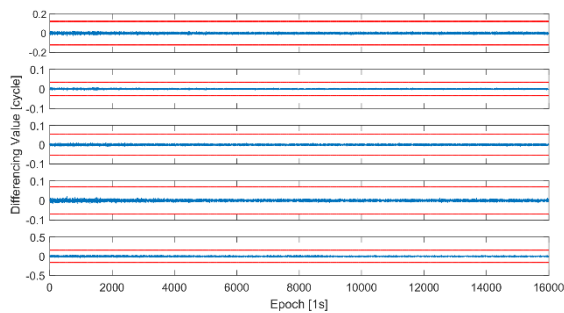**FIGURE 7.** The trajectory of the kinematic experiment.

FIGURE 8. Differencing value of the cycle slip detection combinations for the satellite C21 with no simulated cycle slips. The panels from top to bottom denote the combinations Nos. 1, 2, 3, 4 and 5, respectively.
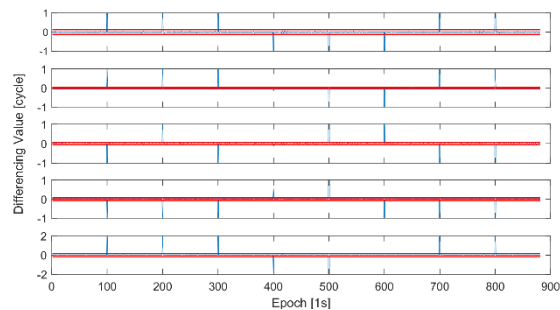

FIGURE 9. Differencing value of the cycle slip detection combinations for the satellite C21 with simulated cycle slips. The panels from top to bottom denote the combinations Nos. 1, 2, 3, 4 and 5, respectively.

search method. Due to the limited space, we only list some cycle slip repair results of the satellites C20 and C39 under six different typical situations (i.e., the cycle slip only occurs on one, two, three, four or five carriers and the equal cycle slip) in Table 7. Since the influence of the observation noise, it can be clearly found that the cycle slip repair success rate
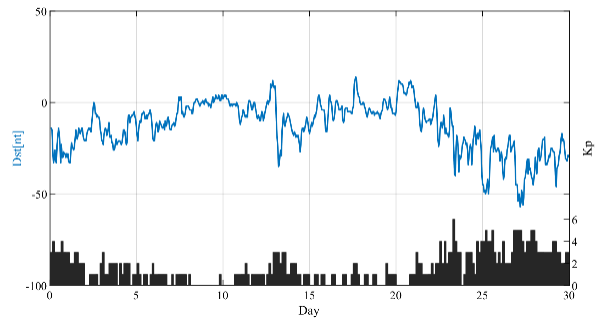

FIGURE 10. The time series of the Dst index and the Kp index for 30 consecutive days in September 2020.
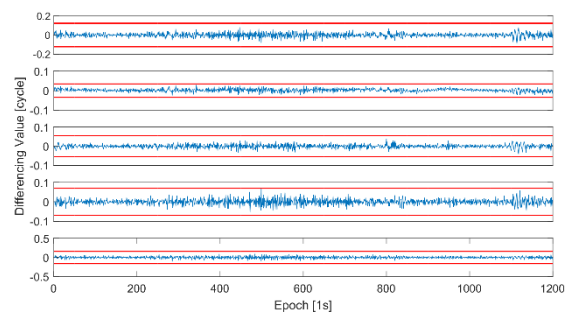

FIGURE 11. Differencing value of the cycle slip detection combinations for the satellite C27 when no cycle slip occurs. The panels from top to bottom denote the combinations Nos. 1, 2, 3, 4 and 5, respectively.

FIGURE 12. Differencing value of the cycle slip detection combinations for the satellite C39 when no cycle slip occurs. The panels from top to bottom denote the combinations Nos. 1, 2, 3, 4 and 5, respectively.
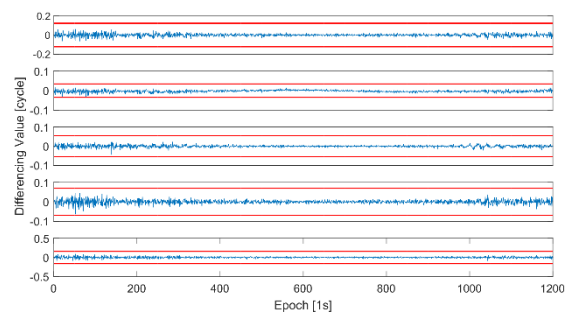
by rounding directly is 94.65% and 97.18%, respectively. But both the ones by using the LAMBDA search method can reach 100%. In brief, the five-frequency cycle slip repair is effectively performed by using the LAMBDA search method. Hence, it can be concluded that the proposed method can detect and repair the cycle slips in real time by combining four geometry-free phase combinations $[4, -5, 1, 5, -5]$ $[1, -2, 1, 1, -1]$ $[1, -1, 1, -3, 2]$ $[-4, 4, 1, -2, 1]$ and one geometry-free phase and pseudorange combination $[1, -1, 0, 1, -1]$.

In order to further test the effectiveness of the proposed cycle slip detection and repair method in kinematic situation, we have collected the real five-frequency kinematic data in campus and the trajectory of kinematic experiment is shown in Figure 7. The data sampling interval is 1 s. Then we select the satellite C21 (MEO) which has the best visibility as an

TABLE 7. The cycle slip repair results with the LAMBDA method under different typical situations.

Epoch	PRN	Cycle slips	$\hat{X}^T$	Repair results
500	C20	(0, 0, 4, 0, 0)	[-0.249, -0.251, 3.794, -0.197, -0.186]	(0, 0, 4, 0, 0)
	C39	(0, 0, 4, 0, 0)	[-0.268, -0.267, 3.783, -0.203, -0.200]	(0, 0, 4, 0, 0)
2625	C20	(0, 4, 1, 0, 0)	[0.142, 4.140, 1.120, 0.114, 0.109]	(0, 4, 1, 0, 0)
	C39	(0, 4, 1, 0, 0)	[-0.370, 3.630, 0.704, -0.280, -0.277]	(0, 4, 1, 0, 0)
4500	C20	(1, 2, 1, 0, 0)	[0.336, 1.345, 0.468, -0.504, -0.494]	(1, 2, 1, 0, 0)
	C39	(1, 2, 1, 0, 0)	[0.890, 1.887, 0.916, -0.086, -0.087]	(1, 2, 1, 0, 0)
5800	C20	(1, 4, 1, 2, 0)	[1.054, 4.063, 1.051, 2.049, 0.043]	(1, 4, 1, 2, 0)
	C39	(1, 4, 1, 2, 0)	[1.044, 4.042, 1.031, 2.031, 0.033]	(1, 4, 1, 2, 0)
7230	C20	(2, 1, 2, 4, 1)	[1.898, 0.898, 1.914, 3.922, 0.920]	(2, 1, 2, 4, 1)
	C39	(2, 1, 2, 4, 1)	[2.005, 1.004, 2.002, 4.004, 1.001]	(2, 1, 2, 4, 1)
11715	C20	(3, 3, 3, 3, 3)	[2.803, 2.799, 2.837, 2.849, 2.846]	(3, 3, 3, 3, 3)
	C39	(3, 3, 3, 3, 3)	[3.292, 3.283, 3.231, 3.218, 3.213]	(3, 3, 3, 3, 3)

TABLE 8. The size and location of the simulated cycle slips.

The location of cycle slip/epoch	The smaller cycle slips groups	The bigger cycle slips groups
100	(0, 1, 1, 5, 1)	/
200	(3, 0, 5, 2, 3)	/
300	(7, 2, 3, 5, 1)	/
400	(1, 2, 3, 5, 6)	/
500	/	(25, 36, 40, 15, 27)
600	/	(37, 33, 18, 22, 26)
700	/	(22, 16, 30, 25, 13)
800	/	(19, 22, 18, 34, 27)

TABLE 9. The cycle slip repair results of the satellites C21.

| Epoch	Cycle slips	$\hat{X}^T$	Repair results
100	(0, 1, 1, 5, 1)	[0.875, 1.879, 1.721, 5.673, 1.645]	(0, 1, 1, 5, 1)
200	(3, 0, 5, 2, 3)	[2.502, -0.484, 4.599, 1.606, 2.624]	(3, 0, 5, 2, 3)
300	(7, 2, 3, 5, 1)	[7.305, 2.299, 3.245, 5.233, 1.222]	(7, 2, 3, 5, 1)
400	(1, 2, 3, 5, 6)	[0.695, 1.707, 2.767, 4.767, 5.785]	(1, 2, 3, 5, 6)
500	(25, 36, 40, 15, 27)	[25.357, 36.358, 40.284, 15.268, 27.266]	(25, 36, 40, 15, 27)
600	(37, 33, 18, 22, 26)	[37.127, 33.138, 18.110, 22.085, 26.087]	(37, 33, 18, 22, 26)
700	(22, 16, 30, 25, 13)	[21.320, 15.318, 29.446, 24.484, 12.493]	(22, 16, 30, 25, 13)
800	(19, 22, 18, 34, 27)	[19.468, 22.466, 18.389, 34.355, 27.356]	(19, 22, 18, 34, 27)
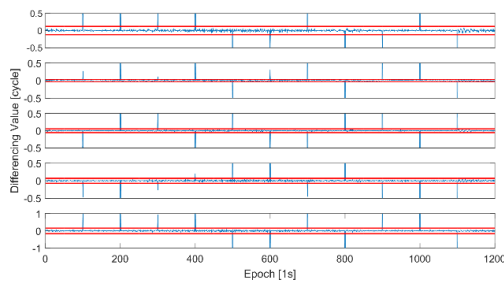
FIGURE 13. Differencing value of the cycle slip detection combinations for the satellite C27. The panels from top to bottom denote the combinations Nos. 1, 2, 3, 4 and 5, respectively.

example. Since there are no cycle slips in raw carrier phase observations which is shown as Figure 8, some simulated cycle slips consist of four smaller and four bigger cycle slips are added to raw carrier phase observations with an interval of 100 epochs, which are listed in Table 8.

Figure 9 illustrate the differencing value of the satellite C21 when the cycle slips occur. It can be clearly found that the differencing value will obviously varies and exceeds the corresponding detection threshold when the cycle slip occurs. And we can find that all the smaller and bigger cycle slips can be detected in the kinematic experiment. Table 9 lists the real-time cycle slip repair results. It can be concluded that all the simulated cycle slips can be repaired correctly in real time by using the proposed cycle slip repair algorithm. Hence, the five-frequency cycle slip detection and repair method can be used to detect and repair the cycle slips in kinematic situation.

C. EXPERIMENT THREE

To further verify the practicality of the proposed method under the condition of active ionospheric and low sampling rate, we select MGEX (Multi-GNSS Experiment) station

TABLE 10. The size and location of the simulated cycle slips.

The location of cycle slip/epoch	The smaller cycle slips groups	The bigger cycle slips groups
100	(1, 3, 1, 5, 1)	/
200	(6, 0, 7, 2, 5)	/
300	(5, 4, 3, 1, 1)	/
400	(1, 2, 7, 5, 1)	/
500	(3, 5, 6, 2, 7)	/
600	(2, 7, 9, 5, 3)	/
700	/	(21, 26, 30, 35, 23)
800	/	(17, 32, 28, 24, 47)
900	/	(37, 29, 31, 19, 25)
1000	/	(26, 15, 33, 37, 20)
1100	/	(44, 37, 24, 35, 48)

TABLE 11. The cycle slip repair results of the satellites C27 and C39 with the LAMBDA method.

Epoch	PRN	Cycle slips	$\hat{X}^T$	Repair results
100	C27	(1, 3, 1, 5, 1)	[1.936, 3.913, 1.765, 5.730, 1.715]	(1, 3, 1, 5, 1)
	C39	(1, 3, 1, 5, 1)	[0.027, 2.017, 0.167, 4.222, 0.226]	(1, 3, 1, 5, 1)
200	C27	(6, 0, 7, 2, 5)	[4.624, -1.378, 5.864, 0.943, 3.972]	(6, 0, 7, 2, 5)
	C39	(6, 0, 7, 2, 5)	[4.393, -1.598, 5.700, 0.753, 3.772]	(6, 0, 7, 2, 5)
300	C27	(5, 4, 3, 1, 1)	[3.432, 2.455, 1.730, -0.202, -0.164]	(5, 4, 3, 1, 1)
	C39	(5, 4, 3, 1, 1)	[4.411, 3.435, 2.495, 0.516, 0.513]	(5, 4, 3, 1, 1)
400	C27	(1, 2, 7, 5, 1)	[1.272, 2.275, 7.210, 5.233, 1.231]	(1, 2, 7, 5, 1)
	C39	(1, 2, 7, 5, 1)	[1.861, 2.857, 7.696, 5.664, 1.643]	(1, 2, 7, 5, 1)
500	C27	(3, 5, 6, 2, 7)	[2.998, 4.970, 6.002, 2.029, 7.039]	(3, 5, 6, 2, 7)
	C39	(3, 5, 6, 2, 7)	[3.595, 5.606, 6.475, 2.455, 7.453]	(3, 5, 6, 2, 7)
600	C27	(2, 7, 9, 5, 3)	[1.056, 6.059, 8.268, 4.310, 2.338]	(2, 7, 9, 5, 3)
	C39	(2, 7, 9, 5, 3)	[1.599, 6.599, 8.683, 4.699, 2.715]	(2, 7, 9, 5, 3)
700	C27	(21, 26, 30, 35, 23)	[21.997, 26.993, 30.829, 35.810, 23.776]	(21, 26, 30, 35, 23)
	C39	(21, 26, 30, 35, 23)	[22.481, 25.487, 29.576, 34.597, 22.607]	(21, 26, 30, 35, 23)
800	C27	(17, 32, 28, 24, 47)	[16.370, 31.360, 27.523, 23.511, 46.575]	(17, 32, 28, 24, 47)
	C39	(17, 32, 28, 24, 47)	[16.956, 31.966, 27.931, 23.930, 46.927]	(17, 32, 28, 24, 47)
900	C27	(37, 29, 31, 19, 25)	[36.903, 28.891, 30.949, 18.954, 24.960]	(37, 29, 31, 19, 25)
	C39	(37, 29, 31, 19, 25)	[37.313, 29.318, 31.233, 19.217, 25.214]	(37, 29, 31, 19, 25)
1000	C27	(26, 15, 33, 37, 20)	[26.149, 15.160, 33.150, 37.154, 20.151]	(26, 15, 33, 37, 20)
	C39	(26, 15, 33, 37, 20)	[26.327, 15.307, 33.240, 37.222, 20.226]	(26, 15, 33, 37, 20)
1100	C27	(44, 37, 24, 35, 48)	[42.884, 35.903, 23.082, 34.143, 47.134]	(44, 37, 24, 35, 48)
	C39	(44, 37, 24, 35, 48)	[43.932, 36.921, 23.902, 34.912, 47.900]	(44, 37, 24, 35, 48)

SGOC (6.89°N and 79.87°E) for this experiment, which locates in a low latitude area quite affected by the ionospheric delays. The data sampling interval is 30 s, which will magnify the differencing ionospheric delays between epochs. Figure 10 depicts the time series of the Dst (Disturbance Storm Tine) index and the Kp index for 30 consecutive days in September, 2020. It can be found that the intense geomagnetic storm occurred on September 28, which the Dst index was around -50 nt and the sum of Kp was 35 on that day. Hence, we select C27 (MEO) and C39 (IGSO) five-frequency observation data of September 28, 2020 as an example to test the proposed algorithm. Because there are no cycle slips in the raw carrier phase data, the six smaller cycle slips and

five bigger cycle slips are artificially added to the raw carrier phase observations with an interval of 100 epochs. The size and location of the cycle slips are listed in Table 10.

Figure 11 and Figure 12 illustrate the differencing value of the satellites C27 and C39 cycle slip detection combinations when no cycle slip occurs. It can be found that the fluctuation range of the geometry-free phase combinations is ±0.09 cycles and the geometry-free phase and pseudorange combinations is ±0.11 cycles, which is larger than that of the experiment one because of the effect of ionospheric delays.

Figure 13 and Figure 14 depict the cycle slips detection results of the satellites C27 and C39, respectively. In addition, the real-time cycle slip repair results are listed in Table 11.
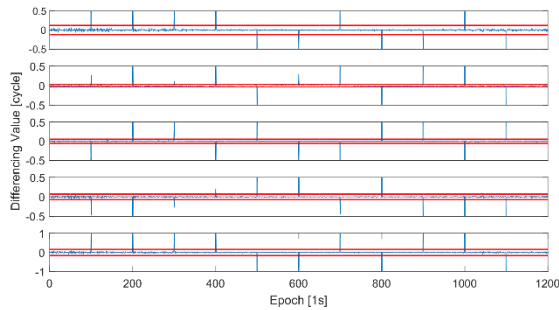
FIGURE 14. Differencing value of the cycle slip detection combinations for the satellite C39. The panels from top to bottom denote the combinations Nos. 1, 2, 3, 4 and 5, respectively.

It can be clearly found that all the manually added cycle slips can be detected and repaired correctly in real time by using the proposed algorithm. Therefore, we can conclude that the five-frequency cycle slip detection and repair method is capable of detecting and repairing the cycle slips under the condition of active ionosphere and low sampling rate in real time.

VII. CONCLUSION

In high-precision positioning applications, the occurrences of cycle slips contaminate carrier phase observations. In this paper, a real-time cycle slip detection and repair method is proposed for BDS-3 five-frequency data. Based on the results and analysis, some conclusions are drawn as follows:

1. Since the geometry-free phase combination is only affected by the phase noise and the ionospheric delay, it can be used to detect the small cycle slips. However, there still remain some undetectable insensitive cycle slip groups for every geometry-free phase combination. Therefore, four joint geometry-free phase combinations $[4, -5, 1, 5, -5]$ $[1, -2, 1, 1, -1]$ $[1, -1, 1, -3, 2]$ $[-4, 4, 1, -2, 1]$ are selected to detect the cycle slips, which have no insensitive cycle slips within the range of $(0, 0, 0, 0, 1)$ to $(50, 50, 50, 50, 50)$.

2. There are more high-quality combinations to select for cycle slips detection and repair with the increasement of frequencies. In addition, the five-frequency high-quality combination has the smallest ionospheric delay effect and noise. The five-frequency geometry-free combination should be better than dual, three and four-frequency combination in terms of cycle slip detection capability and the impact of ionospheric delay reduction.

3. As the five-frequency geometry-free phase combinations are capable of forming only up to four linear independent combinations, one geometry-free phase and pseudorange combination $[1, -1, 0, 1, -1]$ is added to detect and repair the cycle slips. In order to repair the cycle slips with high reliability, the LAMBDA search algorithm is used to repair the cycle slips correctly in real time.

4. The proposed real-time cycle slip detection and repair method can detect and repair all the simulated cycle slips

in real time, even under the condition of active ionospheric and low sampling interval. In summary, the five-frequency real-time cycle slip detection and repair is effectively performed by the proposed method.

Even if encouraging results are obtained, the kinematic field data with real cycle slips requires further investigation in the future.

REFERENCES

[1] G. Xiao, M. Mayer, B. Heck, L. Sui, T. Zeng, and D. Zhao, "Improved time-differenced cycle slip detect and repair for GNSS undifferenced observations," *GPS Solutions*, vol. 22, no. 1, pp. 1–13, Jan. 2018.

[2] B. Ju, D. Gu, X. Chang, T. A. Herring, X. Duan, and Z. Wang, "Enhanced cycle slip detection method for dual-frequency BeiDou GEO carrier phase observations," *GPS Solutions*, vol. 21, no. 3, pp. 1227–1238, Jul. 2017.

[3] G. Blewitt, "An automatic editing algorithm for GPS data," *Geophys. Res. Lett.*, vol. 17, no. 3, pp. 199–202, Mar. 1990.

[4] L. Jing-Nan and G. Mao-Rong, "PANDA software and its preliminary result of positioning and orbit determination," *Wuhan Univ. J. Natural Sci.*, vol. 8, no. 2, pp. 603–609, Jun. 2003.

[5] M. Soycan, "A quality evaluation of precise point positioning within the bernese GPS software version 5.0," *Arabian J. Sci. Eng.*, vol. 37, no. 1, pp. 147–162, Jan. 2012.

[6] Z. Liu, "A new automated cycle slip detection and repair method for a single dual-frequency GPS receiver," *J. Geodesy*, vol. 85, no. 3, pp. 171–183, Mar. 2011.

[7] C. Cai, Z. Liu, P. Xia, and W. Dai, "Cycle slip detection and repair for undifferenced GPS observations under high ionospheric activity," *GPS Solutions*, vol. 17, no. 2, pp. 247–260, Apr. 2013.

[8] M. C. de Lacy, M. Reguzzoni, F. Sansò, and G. Venuti, "The Bayesian detection of discontinuities in a polynomial regression and its application to the cycle-slip problem," *J. Geodesy*, vol. 82, no. 9, pp. 527–542, Sep. 2008.

[9] H.-K. Lee, J. Wang, and C. Rizos, "Effective cycle slip detection and identification for high precision GPS/INS integrated systems," *J. Navigat.*, vol. 56, no. 3, pp. 475–486, Sep. 2003.

[10] S. Banville and R. B. Langley, "Mitigating the impact of ionospheric cycle slips in GNSS observations," *J. Geodesy*, vol. 87, no. 2, pp. 179–193, Feb. 2013.

[11] P. Li, X. Jiang, X. Zhang, M. Ge, and H. Schuh, "Kalman-filter-based undifferenced cycle slip estimation in real-time precise point positioning," *GPS Solutions*, vol. 23, no. 4, pp. 23–99, Jul. 2019.

[12] B. Li, Y. Qin, and T. Liu, "Geometry-based cycle slip and data gap repair for multi-GNSS and multi-frequency observations," *J. Geodesy*, vol. 93, no. 3, pp. 399–417, Mar. 2019.

[13] P. J. G. Teunissen and P. F. de Bakker, "Single-receiver single-channel multi-frequency GNSS integrity: Outliers, slips, and ionospheric disturbances," *J. Geodesy*, vol. 87, no. 2, pp. 161–177, Feb. 2013.

[14] X. Zhang and P. Li, "Benefits of the third frequency signal on cycle slip correction," *GPS Solutions*, vol. 20, no. 3, pp. 451–460, Apr. 2015.

[15] Z. Dai, S. Knedlik, and O. Loffeld, "Real-time cycle-slip detection and determination for multiple frequency GNSS," in *Proc. 5th Workshop Positioning, Navigat. Commun.*, Mar. 2008, pp. 37–43.

[16] L. Huang, Z. Lu, G. Zhai, Y. Ouyang, M. Huang, X. Lu, T. Wu, and K. Li, "A new triple-frequency cycle slip detecting algorithm validated with BDS data," *GPS Solutions*, vol. 20, no. 4, pp. 761–769, Sep. 2015.

[17] G. Chang, T. Xu, Y. Yao, and Q. Wang, "Adaptive Kalman filter based on variance component estimation for the prediction of ionospheric delay in aiding the cycle slip repair of GNSS triple-frequency signals," *J. Geodesy*, vol. 92, no. 11, pp. 1241–1253, Nov. 2018.

[18] Q. Zhao, B. Sun, Z. Dai, Z. Hu, C. Shi, and J. Liu, "Real-time detection and repair of cycle slips in triple-frequency GNSS measurements," *GPS Solutions*, vol. 19, no. 3, pp. 381–391, Jul. 2015.

[19] B. Li, Y. Qin, Z. Li, and L. Lou, "Undifferenced cycle slip estimation of triple-frequency BeiDou signals with ionosphere prediction," *Mar. Geodesy*, vol. 39, no. 5, pp. 348–365, Jun. 2016.

[20] Z. Zhang, B. Li, X. He, Z. Zhang, and W. Miao, "Models, methods and assessment of four-frequency carrier ambiguity resolution for BeiDou-3 observations," *GPS Solutions*, vol. 24, no. 4, pp. 24–96, Jul. 2020.

[21] B. Li, Z. Zhang, W. Miao, and G. Chen, "Improved precise positioning with BDS-3 quad-frequency signals," *Satell. Navigat.*, vol. 1, no. 1, pp. 1–10, Dec. 2020.

[22] S. Jin and K. Su, "PPP models and performances from single- to quad-frequency BDS observations," *Satell. Navigat.*, vol. 1, no. 1, pp. 1–13, Apr. 2020.

[23] *China Satellite Navigation Office. Development of the BeiDou Navigation Satellite System (Version 3.0)*, China Satellite Navigation Office, Beijing, China, 2018.

[24] *China Satellite Navigation Office. Development of the BeiDou Navigation Satellite System (Version 4.0)*, Beijing: China Satellite Navigation Office, Beijing, China, 2019.

[25] J. Li, Y. Yang, H. He, and H. Guo, "Benefits of BDS-3 B1C/B1I/B2a triple-frequency signals on precise positioning and ambiguity resolution," *GPS Solutions*, vol. 24, no. 4, pp. 24–100, Oct. 2020.

[26] Z. Zhang, B. Li, and X. He, "Geometry-free single-epoch resolution of BDS-3 multi-frequency carrier ambiguities," (in Chinese), *Acta Geodaetica et Cartographica Sinica*, vol. 49, no. 9, pp. 1139–1148, Sep. 2020.

[27] P. J. G. Teunissen, "The least-squares ambiguity decorrelation adjustment: A method for fast GPS integer ambiguity estimation," *J. Geodesy*, vol. 70, nos. 1–2, pp. 65–82, Nov. 1995.

XIUFENG HE received the B.S. and M.S. degrees from the Nanjing University of Aeronautics and Astronautics, and the Ph.D. degree from The Hong Kong Polytechnic University. She is currently working as a Professor with Hohai University. Her research interests include satellite geodesy, deformation monitoring, InSAR and multi-source data fusion, and integrated navigation using GNSS and IMU.

TIANYANG XU received the B.S. degree from the College of Surveying and Mapping Engineering, Suzhou University of Science and Technology, China. He is currently pursuing the M.S. degree with the School of Earth Sciences and Engineering, Hohai University. His research interests include low-cost receiver data processing and real-time kinematic positioning.

HAIJUN YUAN received the B.S. degree from the School of Hydraulic and Ecological Engineering, Nanchang Institute of Technology, China. He is currently pursuing the M.S. degree with the School of Earth Sciences and Engineering, Hohai University. His research interests include GNSS precise point positioning and data processing.

XUEYONG XU received the Ph.D. degree from the University of Science and Technology of China. He is currently a Professorate Senior Engineer with North Information Control Research Academy Group Company Ltd., China. His current research interest includes high-precision GNSS applications.

ZHETAO ZHANG received the Ph.D. degree from the College of Surveying and Geo-Informatics, Tongji University, China. He was previously a Research Assistant with The Hong Kong Polytechnic University and a Visiting Ph.D. Student with the University of Calgary. His research interest includes GNSS precise positioning and applications.

NAN ZANG received the Ph.D. degree from the College of Surveying and Geo-Informatics, Tongji University, China. Her current research interest includes multi-GNSS precise point positioning and applications.

● ● ●